



DFT and kinetic evidences of the preferential CO oxidation pattern of manganese dioxide catalysts in hydrogen stream (PROX)

Francesco Arena^{a,b,*}, Francesco Ferrante^{c,**}, Roberto Di Chio^a, Giuseppe Bonura^b,
Francesco Frusteri^b, Leone Frusteri^b, Antonio Prestianni^c, Sara Morandi^d, Gianmario Martra^{d,1},
Dario Duca^c

^a Dipartimento di Ingegneria, Università di Messina, C.da Di Dio, I-98166 S. Agata, Messina, Italy

^b Istituto CNR-ITAE "Nicola Giordano", Salita S. Lucia 39, I-98126 S. Lucia, Messina, Italy

^c Dipartimento di Chimica e Fisica "Emilio Segrè", Università di Palermo, V.le delle Scienze Ed. 17, I-90128 Palermo, Italy

^d Department of Chemistry and Centre for "Nanostructured Interfaces and Surfaces-NIS", Università di Torino, Via P. Giuria 7, I-10125 Torino, Italy

ARTICLE INFO

Keywords:

DFT analysis
H₂ and CO oxidation
Manganese dioxide catalyst
Reaction mechanism and kinetics
Preferential CO oxidation

ABSTRACT

The oxidation functionality of Mn(IV) sites has been assessed by density functional theory (DFT) analysis of adsorption and activation energies of CO, H₂ and O₂ on a *model* Mn₄O₈ cluster. DFT calculations indicate that Mn (IV) atoms prompt an easy CO conversion to CO₂ via a reaction path involving both catalyst and gas-phase oxygen species, while much greater energy barriers hinder H₂ oxidation. Accordingly, a MnCeO_x catalyst (Mn_{at}/Ce_{at} 5) with large exposure of Mn(IV) sites shows a remarkable CO oxidation performance at T ≥ 293 K and no H₂ oxidation activity below 393 K. Empiric kinetics disclose that the catalyst-oxygen abstraction step determines both CO and H₂ oxidation rate, although different activation energies favor the preferential oxidation (PROX) pattern of the studied catalyst (353–423 K). Conversion-selectivity of 100%, high stability during 72 h reaction time and moderate inhibiting effects of water and CO₂ feeding reveal the potential of MnO₂ materials as efficient, low-cost and robust PROX catalysts.

1. Introduction

Nowadays the hydrocarbons and alcohols reforming is the leading technology for hydrogen production, although the cogeneration of large amount of CO hinders a straight feeding of the reformate streams to polymeric-electrolyte-membrane fuel cells (PEMFC), hydrogenation and ammonia synthesis plants, because of remarkable catalyst poisoning issues [1]. Thus, water gas shift units reduce the CO content to ca. 1%, while a final cut (<50 ppm) is ensured by methanation, membrane separation or preferential CO oxidation (PROX) units [1]. Despite the latter is a more suitable option for small-medium scale H₂ purification and integration with PEMFC devices, however, the lack of efficient and robust catalysts remains the main drawback of the PROX technology [1–3].

Catalysts currently under scrutiny include noble metals, gold-nanoparticles and transition metals/oxides, but none of these still

fulfils the requirements for commercial exploitation [2,3]. In fact, nanoporous Au nanoparticles show excellent activity in the CO oxidation at T < 373 K [4], while Au-clusters (≤2 nm) supported on reducible oxide carriers prompt the H₂ oxidation via the stepwise Mars–van Krevelen mechanism, depressing the CO₂ selectivity at high temperature [5,6]. At variance, noble-metals (e.g., Pt, Rh, Ir, Ru) triggers the CO oxidation via a Langmuir–Hinshelwood (L-H) reaction pathway that is poorly efficient at low temperature since strong CO chemisorption hinders the dissociative adsorption of O₂; on the other hand, a high reactivity towards H₂ determines low selectivity standards at T > 373 K [2,3]. Thus, staggering advances in the PROX performance of noble-metal catalysts are due to promoters or carriers prompting *dual-site* reaction mechanisms [2,3,7–18]. On this account, the successful strategies encompass: i) the alloying/decoration of metal particles with metal/oxide species to improve the surface O₂-activation functionality [2,3,7–14]; ii) the weakening of metal-CO bond by

* Corresponding author at: Dipartimento di Ingegneria, Università di Messina, C.da Di Dio, I-98166 S. Agata, Messina, Italy.

** Corresponding author.

E-mail addresses: Francesco.Arena@unime.it (F. Arena), Francesco.Ferrante@unipa.it (F. Ferrante).

¹ Notes: G.M., deceased on Sept. 29th 2020.

alkali-promoters' addition [2,3,15] or by chemical tuning of active sites [16]; and iii) the use of carriers with high mobility of oxygen atoms or hydroxyl groups [17,18]. However, the efficiency of such materials relies on accurate design and control of active sites, deserving complex and time-consuming synthesis procedures [3–5,7–18].

Hence, great research efforts are currently devoted to catalyst formulations including transition metals and metal oxides because of remarkable advantages with respect to noble metals, like great availability, low-cost and peculiar catalytic properties due to the reactivity of oxide, sub-oxide and metal phases [19–25]. Despite catalysts including copper [19–22,25] and cobalt [23,24] show good PROX performance at $T > 373$ K, the reaction environment has a decisive influence on the activity-selectivity pattern [19–25]. For instance, Cu-based catalysts could show an improved activity in presence of water and CO_2 containing feedstocks [19–22], while a recent study shows that the PROX functionality of the CuCeO_x system depends on metal Cu sites that are unstable under complete CO conversion conditions [25]. Likewise, the surface oxidation state is decisive for Co catalysts, due to the “blocking-effect” of carbonate species on the reactivity of the Co_3O_4 phase [23]. At variance, the PROX behavior of manganese oxides remains still unknown, although their promoting effect on the activity-selectivity pattern of both Cu and Co catalysts [20,22,24] and a relevant CO oxidation performance at low temperature ($T < 473$ K) [26–31]. This has been related to the crystal phase, structure and morphology [27–29], while ceria promotes the catalyst surface area and the MnO_x dispersion, forming also very reactive substitutional solid solution centres enhancing the activity at high ceria loading ($\text{Ce}_{\text{at}}/\text{Mn}_{\text{at}} > 0.4$) [26, 30–34]. In spite of this, however, we found that a great availability of Mn(IV) sites renders the bare MnO_2 system more active than composite MnCeO_x catalysts in the CO oxidation [26,30,34] and the selective oxidation of benzyl alcohol with O_2 [35].

Therefore, taking advantage of the support of first-principles models to the understanding of the atomistic clues of catalytic reactions [36], a comparative DFT study of the reactivity of a *model* Mn_4O_8 cluster towards CO and H_2 , in presence and absence of O_2 , has been performed. According to the predicted CO preferential oxidation pattern of Mn(IV) atoms, we show that a MnCeO_x catalyst with large availability of Mn(IV) sites exhibits a high CO oxidation activity and no reactivity towards H_2 in the range of 293–393 K. Consistent with the micro-kinetic analysis of the elementary reaction steps, empiric kinetics show that different mechanisms and activation energies enable the remarkable PROX behavior of the studied catalyst in the range of 353–423 K.

2. Materials and methods

2.1. Computational analysis

All calculations were performed by using the Gaussian 09 package [37]. Density functional theory was used by selecting the M06-L exchange-correlation functional of Thrular's group [38]. The Stuttgart '97 Relativistic Small Core effective potential and corresponding valence double zeta basis set for the Mn atoms [39], coupled with the cc-pvDZ basis set for lighter elements, complete the model chemistry. The geometries of minima and transition states have been fully optimized and characterized by inspection of the calculated harmonic vibrational frequencies. In the following, all energies are intended to contain the vibrational zero-point contribution. The M06-L functional was chosen because it is explicitly parametrized to give good performance for transition metal chemistry, in particular when dispersion interactions may have an important role (e.g. in the adsorption process). Just like all other functionals by Minnesota groups, the reliability of M06-L was tested against an extensive number of databases and, thanks to its performance, it represents the best choice for the energetics of compounds containing transition metals [40]. By collecting the results of a number of studies [41–43], an averaged mean unsigned error of ca. $10 \text{ kJ}\cdot\text{mol}^{-1}$ can be estimated for barrier heights of reactions involving

transition metals. The oxidation reactions of CO and H_2 were simulated using a Mn_4O_8 model cluster; the characteristics of its geometric and electronic structures, as well as the motivation for this choice were outlined in a previous work [36]. The variation of spin multiplicity along the investigated reaction paths, possibly due to spin coupling/decoupling in the involved molecular species and transition states, was checked in all cases and the most stable outcome was selected.

2.2. Materials

A MnCeO_x catalyst at Mn/Ce atomic ratio of 5 (M5C1) was prepared by the *redox-precipitation* synthesis technique [26,30]. In particular, a 10 g sample of the M5C1 catalyst was obtained by titration in acidic solution (pH, 4.5) at 343 K of the $\text{Mn}(\text{NO}_3)_2 \cdot 4 \text{H}_2\text{O}$ salt (0.2 L, 0.25 M) with an aqueous solution (0.2 L) of the KMnO_4 (0.165 M) and Ce $(\text{NH}_3)_2(\text{NO}_3)_6$ (0.085 M) precursors. After titration the solid was digested, filtered, washed with hot distilled water, dried and calcined at 673 K (6 h). The main physico-chemical properties of the M5C1 material are listed in Tab. S1 of SI.

2.3. Characterization methods

X-Ray Fluorescence (XRF) analysis was performed to obtain the chemical composition of the catalyst. The specific surface area, the pore volume and the average pore diameter data were obtained by elaboration of the nitrogen adsorption isotherm (77 K) according to the BET and BJH methods. The *X-Ray Diffraction* (XRD) pattern in the range of $10\text{--}80^\circ$ was obtained by a Philips X-Pert diffractometer at a scan rate of $0.1^\circ\cdot\text{min}^{-1}$, using the Ni β -filtered Cu K_α radiation (40 kV; 30 mA). The *Raman Scattering* spectroscopy analysis was performed using a He-Ne laser (λ , 632.8 nm) at a power beam of 30 μW , focused on the sample by a $50\times$ objective at long focal distance over a 1.5 μm diameter spot, with a resolution of 3 cm^{-1} . *X-ray Photoelectron Spectroscopy* (XPS) data were obtained using a Physical Electronics GMBH PHI 5800–01 spectrometer, operating with a mono-chromatized Al- K_α radiation (300 W). The BE regions of Mn_{2p} (635–680 eV), Ce_{3d} (870–935 eV) and O_{1s} (525–535 eV) were calibrated with reference to the C_{1s} line (284.8 eV) of adventitious carbon. *Temperature Programmed Reduction* measurements in the range of 293–1073 K were performed using a quartz microreactor (i.d. 4 mm; l. 200, mm) containing 20 mg of catalyst, which was fed with 5% H_2/Ar (H_2 -TPR) or 5% CO/He (CO -TPR) carriers (F, 60 $\text{stp mL}\cdot\text{min}^{-1}$) and heated at the rate of $12 \text{ K}\cdot\text{min}^{-1}$. The oxygen *Temperature Programmed Desorption* (O_2 -TPD) test was carried out under the same conditions of TPR analyses, using He as carrier gas (60 $\text{stp mL}\cdot\text{min}^{-1}$) and a QMS (Hiden Analytical, HPR 20) as analytical tool to detect O_2 (m/z , 32), He (m/z , 4), H_2O (m/z , 18) and CO_2 (m/z , 44). *SEM* analysis was performed by a TESCAN S9000G microscope equipped with Schottky source and energy-dispersive X-ray (EDX) detector (OXFORD Ultim Max, Software AZTEC), operating at 15 kV. *TEM* analyses were performed by a PHILIPS CM12 microscope, with high resolution camera and operated at 120 kV, using a catalyst sample ultrasonically dispersed in isopropanol and deposited over a carbon-film supported on a standard Cu-grid.

2.4. Activity testing

The CO and H_2 oxidation activity of the M5C1 catalyst in the range of 293–533 K was probed by temperature programmed reaction tests at heating rate of $2 \text{ K}\cdot\text{min}^{-1}$. The tests were carried out at atmospheric pressure (P , 100 kPa) using the above quartz micro-reactor containing 20 mg of catalyst diluted with granular SiC (w/w, 1/5) and fed at the rate of 60 $\text{stp mL}\cdot\text{min}^{-1}$ (GHSV, $180,000 \text{ h}^{-1}$). The reaction streams containing He as diluent were obtained varying the CO, H_2 and O_2 concentration either in the range of 1.0–2.5%, keeping both CO/O_2 and H_2/O_2 ratio equal to 1, or between 0.625% and 2.5% to vary both CO/O_2 and H_2/O_2 ratio in the range of 0.25–4.0.

Under such conditions, the ideal kinetic regime of measurements has been previously confirmed by the lack of any mass transfer resistances in the whole conversion range [26,31,33].

PROX tests under ideal kinetic conditions were carried out at the above conditions (GHSV, 180,000 h⁻¹), varying the CO and O₂ concentration between 1% and 2% (CO/O₂, 1) and that of H₂ between 60 (H₂/CO, 60) and 20% (H₂/CO, 10), respectively.

The reaction stream was analyzed *on line* by a QMS (*Hidden Analytical*, HPR 20), acquiring the signals of H₂ (*m/z*, 2), He (*m/z*, 4), H₂O (*m/z*, 18), CO (*m/z*, 28), O₂ (*m/z*, 32) and CO₂ (*m/z*, 44) in multiple ion detection (MID) mode. Conversion data (*X*), obtained by the *internal standard* (1) and *mass balance* methods (2) respectively,

$$X_{IS} = 1 - \frac{(p_{\text{reag}}/p_{\text{He}})_T}{(p_{\text{reag}}/p_{\text{He}})_{273K}} \quad (1)$$

$$X_{MB} = \frac{(p_{\text{prod}})_T}{(p_{\text{reag}} + p_{\text{prod}})_T} \quad (2)$$

were in good agreement and reproducible ($\pm 5\%$) [31,33,36]. Further, since no CH₄ formation was detected, CO₂ selectivity data under PROX conditions were obtained by the formula (3)

$$S_{\text{CO}_2} = \frac{(2 \cdot X_{\text{O}_2})}{(X_{\text{CO}})} \quad (3)$$

PROX measurements under integral conversion conditions were also carried out using a tubular reactor (i.d., 13 mm; l., 250 mm), jacketed with a stainless-steel rod (o.d., 30 mm) for minimizing temperature gradients. The reactor was loaded with 1–5 g of catalyst (16–25 mesh), diluted with same sized α -Al₂O₃ (GHSV, 720–3600 h⁻¹) and fed with a reaction mixture (P, 100 kPa) containing CO (1%), O₂ (1%), H₂ (85%) and N₂ (13%) as internal standard. Moreover, the effects of water (4%) and CO₂ (10%) in the feed (CO, 1%; O₂, 1%; H₂, 70%; N₂, 14%) have been also assessed. The reactor stream has been analyzed *on-line* by a GC (HP5890 Series II Plus), equipped with a dual-column system and connected to a TCD for detection of O₂, N₂, CO and CO₂. The stream was also scanned by a Modular Process Analysis System (ABB Instrument), operated with a twin-beam no dispersive IR-photometer (URAS 14 module analyzer) for CO and CO₂ quantification.

Before testing, catalyst samples were preliminarily treated *in situ* at 423 K in 5% O₂/He flow (1 h).

3. Results and discussion

3.1. DFT analysis of adsorption and reaction of CO, H₂ and O₂ on the model Mn₄O₈ cluster

The DFT analysis of the oxidation functionality of Mn(IV) sites

towards CO and H₂ has been carried out considering a *model* Mn₄O₈ cluster, previously adopted for modelling the reactivity pattern of MnO₂ catalysts in the selective aerobic oxidation of benzyl alcohol [36]. In the most stable configuration this is characterised by high spin (2 S+1 = 13) C_{2h} symmetry, including two topologically different Mn(IV) sites, labelled Mn(A) and Mn(B) respectively (inset of Fig. 1).

The Mn(A) centres share two of four oxygen atoms having a distorted disphenoidal arrangement, similar to SF₄, with the equatorial plane tilted by ca. 20°. The geometry around the Mn(B) atom is a strongly distorted tetrahedral, with O-connections to each of the Mn(A) sites and one dangling oxygen atom. In order to consider spin coupling/decoupling processes along the reaction paths, all the intermediates and transition states were investigated considering 2 S+1 = 11, 13, and 15 spin multiplicities and selecting, in any case, the lowest energy state.

The CO molecule preferentially adsorbs on the Mn(A) site, with an interaction energy of 85.5 kJ mol⁻¹, since the adsorption on the Mn(B) site implies an energy release of only 25.2 kJ mol⁻¹. In both cases the interaction occurs from the C-side with top adsorption geometry, leaving an unchanged C-O bond length despite a C-Mn distance of 2.115 and 2.178 Å is calculated for the interaction of CO with Mn(A) and Mn(B) sites, respectively.

Also the O₂ molecule should preferentially adsorb on the Mn(A) centre of the cluster, being the adsorption energy equal to - 92.0 kJ mol⁻¹, a value which is 65 kJ mol⁻¹ lower than the adsorption energy on Mn(B). In the first case, a μ_2 bridged adsorption geometry produces a sensible O—O bond stretching (Mn-O distance is 1.992 Å and the O-O one is 1.277 Å), while a top adsorption mode (with Mn-O and O-O equal to 2.266 and 1.214 Å, respectively) occurs in the other case.

Despite the stronger adsorption energies, further calculations show that none of the reaction paths involving the Mn(A) atom is feasible. Indeed, the shift of an oxygen atom from the cluster to CO adsorbed on Mn(A) implies an energy barrier of ca. 300 kJ mol⁻¹ (see Fig. S1 of SI) because the neighbouring O-atoms are very strongly bonded to the cluster frame. The adsorption of an O₂ molecule on a Mn(A) site where CO is already adsorbed occurs with an energy release of 44.9 kJ mol⁻¹ while, reversing the species (i.e. CO adsorbs on O₂/Mn₄O₈), an energy release of 38.5 kJ mol⁻¹ is calculated. Notably, these values are much smaller than the corresponding ones in absence of co-adsorption. The formation of CO₂ starting from this (CO+O₂)/Mn₄O₈ configuration (Fig. S2 of SI) shows an energy barrier of 102.8 kJ mol⁻¹. On the other hand, the adsorption of O₂ on the Mn(A) site adjacent to the one where CO is adsorbed releases 93.7 kJ mol⁻¹; nevertheless, in this case the reaction between the two coadsorbed species can safely be ruled out, since they are too far from each other.

Therefore, the favoured reaction paths involve only the Mn(B) site of the cluster. In fact, the formation of the first CO₂ molecule (Fig. 1, left) occurs by the shift of the dangling oxygen of the Mn(B) atom to the adsorbed CO, overcoming an energy barrier of 52.1 kJ mol⁻¹. This leaves

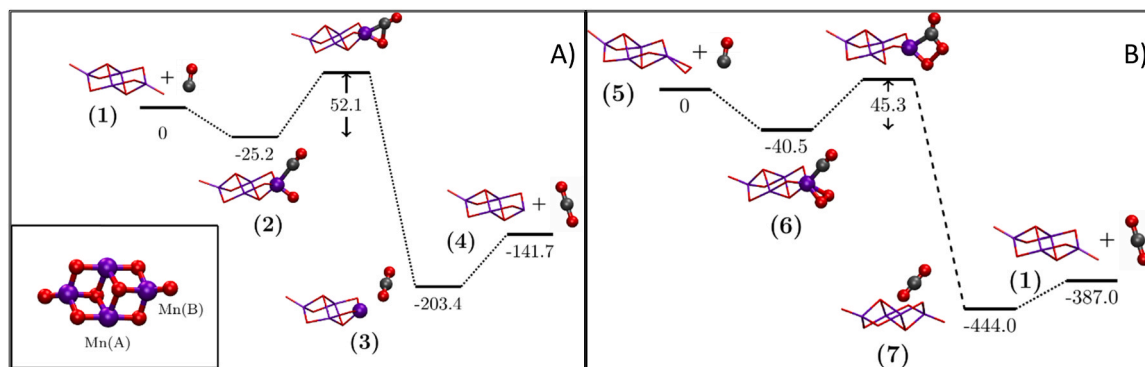


Fig. 1. DFT energy (kJ mol⁻¹) diagrams for the oxidation of the first CO molecule on the Mn(B) site of the Mn₄O₈ cluster (A) and the second CO molecule on the O₂-Mn₄O₇ intermediate (B). Mn (purple), O (red), C (grey) atoms involved in the reaction steps are highlighted, while numbers in brackets refer to the various intermediates. For reference, the *model* Mn₄O₈ cluster, along with the labelling used for Mn centres, is shown in the inset of panel (A).

an O-vacancy on the Mn(B) atom that prompts the adsorption of O₂ (with 93.0 kJ mol⁻¹ of energy release) and CO, forming the 2nd CO₂ molecule and restoring the Mn₄O₈ cluster (Fig. 1, right).

An alternative reaction path (Fig. S3 of SI) involving the Mn(A) atom could imply the adsorption and fragmentation of O₂ on the Mn₄O₇ cluster leaving adsorbed O-atoms on Mn(A) and Mn(B) sites. However, even if the adsorption of CO on Mn(A) occurs by releasing a large quantity of energy and CO₂ formation is now easier (being 104.2 kJ mol⁻¹ the barrier for the shift of the O atom toward CO), an energy barrier of 152.6 kJ mol⁻¹ for the O₂ fragmentation confirms that the oxidation of both CO molecules occurs on the Mn(B) site of the cluster.

The reaction mechanism occurring on the Mn(B) site was calculated also in presence of a “spectator” CO molecule adsorbed on the Mn(A) centre of the Mn₄O₈ cluster. An analysis of the corresponding data (schematically reported in Fig. S4 of SI) reveals that CO co-adsorption has very small effect on the energetics of the CO oxidation reaction and, in particular, on the energy barriers. The most significant difference is a decrease by ca. 12 kJ mol⁻¹ of the interaction energy between CO and the Mn(B) site of O₂-Mn₄O₇. On the other hand, when the O₂ molecule is considered as spectator on the Mn(A) site (Fig. S5 of SI), a halving of CO adsorption energy on the Mn(B) centre is calculated, along with a corresponding decreasing of the first energy barrier.

Therefore, Fig. 1 summarizes a reaction cycle similar to that predicted by DFT+U analysis for a Mn(IV)-doped CeO₂ system, although in that case the formation of the first CO₂ molecule implies the reduction of neighbouring Ce(IV) atoms [32]. In particular, a micro-kinetic model specifically designed to manage kinetic analyses by quantum chemistry descriptors (SCM) [44,45] indicates that the cycle should be characterised by an activation energy of ca. 60 kJ mol⁻¹ in the range of 343–533 K.

At variance, the lack of interaction with the Mn(B) atom hinders the H₂ adsorption and the formation of water by abstraction of the dangling oxygen atom. Although much smaller than those found for CO and O₂, an adsorption energy of –21.5 kJ mol⁻¹ suggests that H₂ would preferentially interact with the Mn(A) atom. The calculated path for H₂ oxidation considering the co-adsorption of H₂ and O₂ on the Mn(A) site of the Mn₄O₈ cluster is reported in Fig. S6 of SI. In this case, the adsorption of H₂ on the O₂/Mn₄O₈ adduct occurs with an energy release of 12.4 kJ mol⁻¹, implying negligible change in the H–H and O–O bond length in comparison to the isolated molecules. Hence, the Mn(A) site

drives the H₂ oxidation to very low extents because of four energy barriers, two of which are in the order of 150 kJ mol⁻¹.

Alternative reaction paths elucidating potential reciprocal effects between H₂ and CO oxidation start from the reduced (i.e., Mn₄O₇) and over-oxidized (i.e., O₂-Mn₄O₇) forms of the Mn₄O₈ cluster, since under co-feeding conditions these occur in the steps 3→4 and 4→5 of the CO oxidation network (Fig. 1). This point will be discussed in more detail later since on the real catalyst such intermediates could be also generated by oxygen spillover phenomena among neighbouring Mn(IV) sites.

The DFT analysis shows that the surface reaction path on the O₂-Mn₄O₇ intermediate implies a preliminary adsorption of H₂ (step 5→8) with an energy release of 20.8 kJ mol⁻¹ (Fig. 2). This does not produce any sensible stretching of the O–O bond and the weak interaction between adsorbed species is probed by an energy barrier of 106.6 kJ mol⁻¹ for the formation of the first (OOH)H-Mn₄O₇ intermediate (step 8→9). After rearranging its geometry (step 9→10), this forms a (OHOH)Mn₄O₇ intermediate overcoming an energy barrier of 100.2 kJ mol⁻¹ (step 10→11). In turn, this favours the H-shift leading to the formation of H₂O (step 11→12) and the replenishment of the Mn₄O₈ cluster (step 12→1). Although this account for the H₂ oxidation on the O₂-Mn₄O₇ intermediate, DFT calculations indicate that this route is not competitive with the oxidation of the 2nd CO molecule owing to much weaker adsorption and higher reaction barriers. Possible ramifications of the path from intermediate 9–12 are reported in Fig. S7 of SI.

In fact, the SCM analysis indicates an activation energy in the range of 343–533 K higher than that of CO oxidation by ca. 35 kJ mol⁻¹, substantiating a typical CO PROX behaviour of O₂-Mn₄O₇ centres in presence of H₂. Indeed, theoretical calculations indicate that the presence of *spectator* CO or O₂ molecules on the Mn(A) site of the O₂-Mn₄O₇ adduct (Fig. S7 of SI) lowers the adsorption energy of H₂ on Mn(B) to few kJ mol⁻¹, but it has no beneficial effects on the first energy barrier.

Finally, the DFT analysis indicates that also the adsorption on the Mn₄O₇ fragment occurs with an energy release of 29.4 kJ mol⁻¹, leading to the conclusion that H₂ interacts with “activated” forms (i.e., Mn₄O₇ and Mn₄O₉) of the Mn₄O₈ cluster.

3.2. Structure and redox properties of the “fresh” catalyst

A Ce-doped MnO_x catalyst (Mn_{at}/Ce_{at}, 5) has been synthesised as experimental counterpart of the model Mn₄O₈ cluster to assess the real

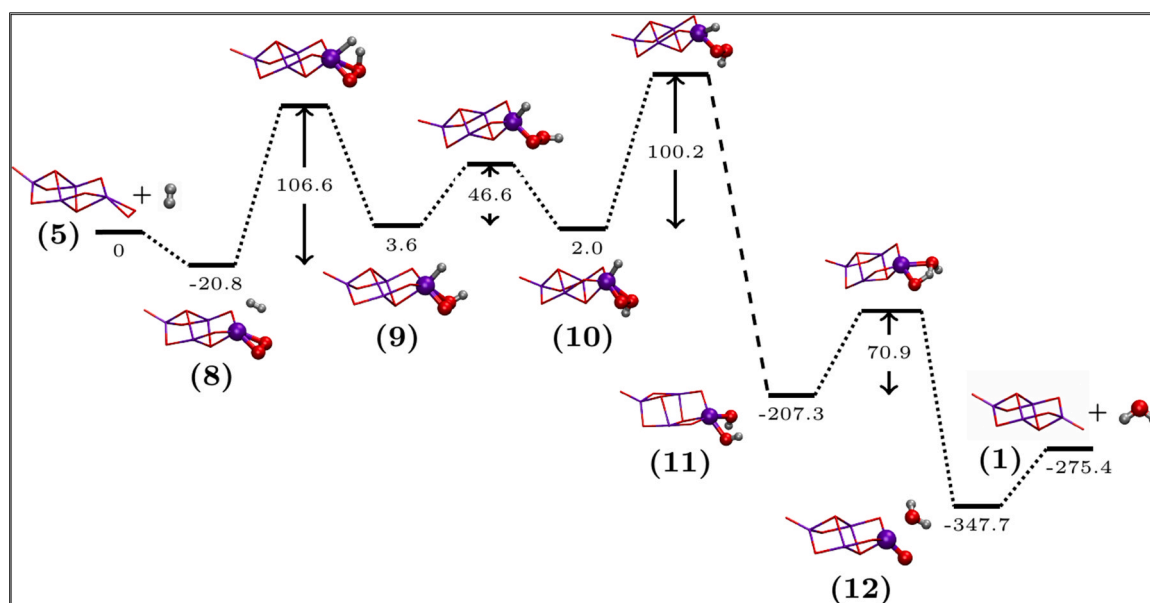


Fig. 2. DFT energy (kJ mol⁻¹) diagram of the H₂ oxidation pathway on the Mn(B) atom of the O₂-Mn₄O₇ adduct. Mn (purple), O (red) and H (white) atoms involved in the reaction steps are highlighted, while numbers in brackets refer to the various intermediates.

functionality of Mn(IV) centres towards CO and H₂. This catalyst formulation (M5C1) has been devised in the light of previous studies showing that ceria exerts remarkable structural effects at low loading ($\text{Ce}_{\text{at}}/\text{Mn}_{\text{at}} < 0.4$), mostly promoting the exposure of active Mn(IV) sites [26,30,34,35,46].

SEM analysis shows that the M5C1 material consists of particles agglomerates with sponge-like morphology (Fig. 3, top left), well accounting for large surface area ($159 \text{ m}^2 \cdot \text{g}^{-1}$) and pore volume ($0.55 \text{ cm}^3 \cdot \text{g}^{-1}$) and a mesoporous texture characterized by an average pore diameter of 30 nm (Tab. S1 of SI). In turn, the low magnification TEM picture displays that catalyst particles include a tangled array of ribbon-rod shaped structures, typical of MnO₂ polymorphs (Fig. 3, top centre), while at high magnification a prevalently amorphous arrangement of the oxide phases is evident (Fig. 3, top right) [27–30,46–48]. Herein the presence of ordered nanodomains with *d*-spacing of 0.71 nm and 0.24 nm signals the incipient genesis of the $\langle 001 \rangle$ and $\langle 100 \rangle$ crystal planes of the δ -MnO₂ phase [46–48], while crystalline nuclei with *d*-spacing of 0.31 nm reveal also the sparse presence of ceria clusters closely embedded into the MnO_x phase [30,46].

Overall an unresolved XRD pattern confirms the lack of significant long-range crystalline order in the M5C1 material (Fig. 3, bottom left) and, in turn, a high dispersion of the oxide phases that is evident from the uniform, Mn-enriched, atom distribution probed by SEM-EDX analysis (Tab. S1 and Tab. S2 of SI). Considering the high sensitivity

of the LR spectroscopy to the short-range structure of surface species, the absence of any characteristic F_{2g} signal of cerianite ($\sim 460 \text{ cm}^{-1}$) in the spectrum of the M5C1 catalyst unveils, in fact, that ceria is mostly incorporated into the MnO_x phase [30,46]. This hinders the layer-to-tunnel transition from δ to the α -MnO₂ phase, favouring the stabilization of birnessite nanodomains responsible of the broad Raman peaks at 502, 573 and 651 cm^{-1} (Fig. 3, bottom left) [26,27,30,46–48].

The XPS analysis definitively substantiates the structural pattern of the M5C1 catalyst, showing a surface Mn/Ce atomic ratio larger than bulk composition (Fig. 3, bottom centre) and Mn peaks characterized by energy-split values (Fig. S9 of SI) typical of MnO₂ polymorphs (Tab. S4 of SI) [27–29,46–49]. In fact, the deconvolution analysis of the Mn_{2p} peak indicates a prevalent fraction of Mn(IV) atoms (Fig. S10 of SI) that, coupled to minor amounts of Mn(III)–Mn(II) atoms (Fig. 3, bottom centre), overall accounts for a Mn average oxidation number of + 3.67 [26,30,46,47,49].

In turn the surface Mn(IV) atoms control the redox functionality of the M5C1 catalyst, although a crucial influence of the reducing species is evident from the CO-TPR and H₂-TPR patterns (Fig. 3 bottom, right). Despite both profiles include a main peak partly convoluted with a small component at higher temperature, a gap of ca. 100 K in the onset reduction and 1st-maximum temperature proves a much stronger reactivity of the M5C1 catalyst towards CO. The first peak monitors the reduction of surface Mn(IV) atoms, while the second is due to reduction

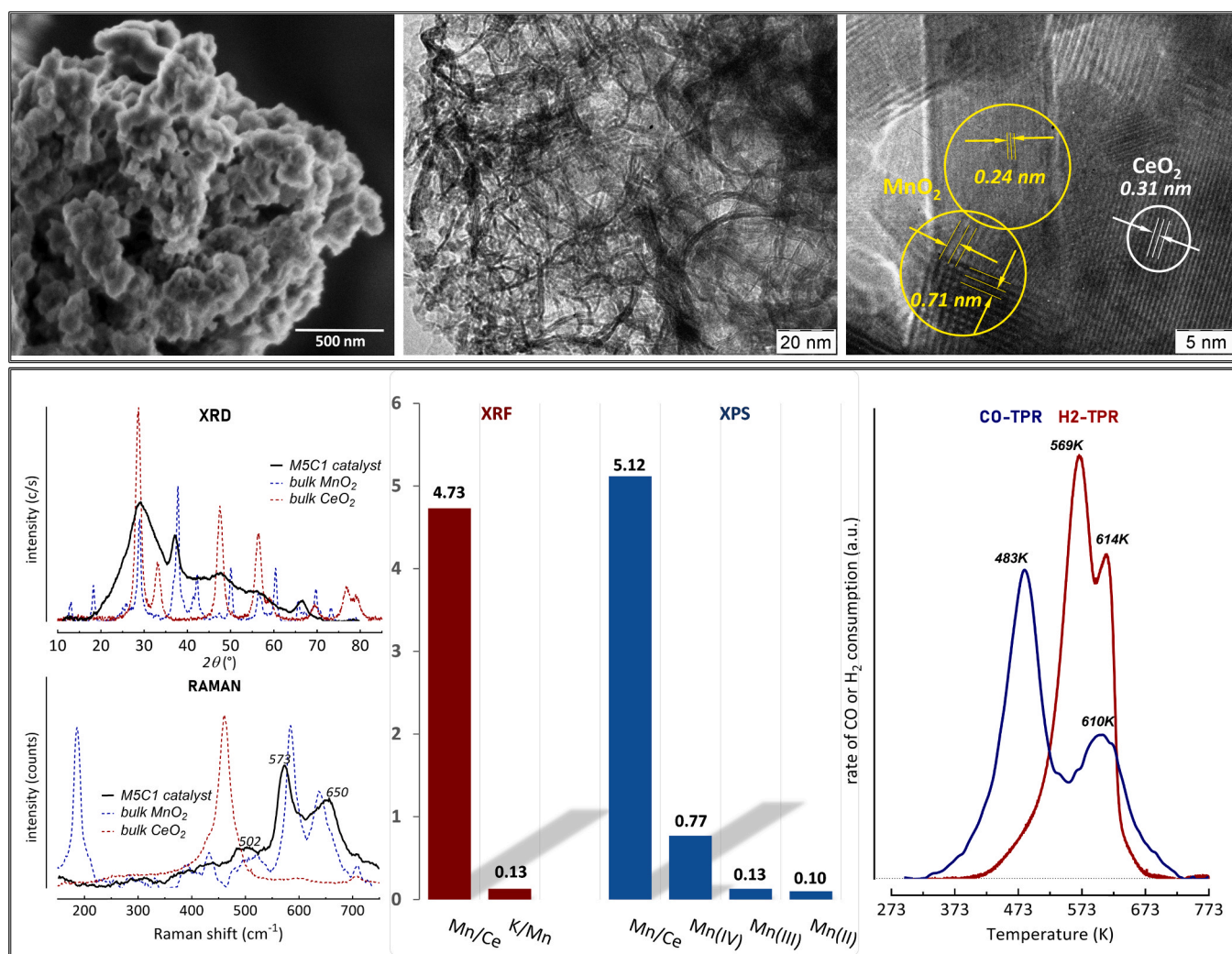


Fig. 3. Characterization data of the “as received” M5C1 catalyst: SEM (top left) and TEM pictures at different magnification (top centre and right); XRD pattern and Laser Raman spectrum (bottom left); bulk (XRF) and surface (XPS) chemical composition data (bottom centre); CO-TPR and H₂-TPR patterns (bottom right).

of bulk MnO_x species ($1 < x \leq 1.5$), resulting insensitive to the reductant [26,30,34]. Considering that such a reduction pattern is analogous to that of the bulk MnO_2 system (see Fig. S11 of SI), it can be argued that ceria favours the surface availability of Mn(IV) sites without affecting their intrinsic reactivity [26,30,34]. On the other hand, the reduction of ceria mostly occurs at $T > 773$ K (Fig. S11 of SI) and, thus, similar extents of CO and H_2 consumption in the range of 293–723 K indicate a Mn average oxidation number of $3.62 (\pm 0.1)$, in agreement with XPS data.

Thus, characterization data confirm that Mn(IV) sites shape the redox functionality of the M5C1 catalyst, substantiating its suitability as experimental counterpart of the model Mn_4O_8 cluster.

3.3. CO and H_2 oxidation activity and reaction kinetics

CO and H_2 oxidation activity tests were carried out under “ideal kinetic conditions”, varying the overall reagents concentration (2–5%), at constant (1.0) substrate/ O_2 ratio (Fig. 4 A, B), and the substrate/ O_2 ratio in the range of 0.25–4.0 (Fig. 4 A', B').

In spite of the high GHSV ($180,000 \text{ h}^{-1}$), the M5C1 catalyst shows a noticeable CO oxidation activity, according to conversion values rising from 0 to final values of 0.5–1.0 in the range of 293–533 K, consistently with the CO/ O_2 ratio. Specifically, conversion data at different reagents concentration (CO/ O_2 , 1) depict overlapping sigmoidal-shaped trends rising from 0 to 1.0 (Fig. 4 A), which are clearly diagnostic of overall 1st-order reaction kinetics.

This is consistent with data at different CO/ O_2 ratio (Fig. 4 B), since conversion values rising at lower p_{CO} and higher p_{O_2} signal reaction orders between 0 and 1 with respect to CO and O_2 .

Onset reaction temperatures higher than 393 K and final conversion values (533 K) lower than 0.25 (Fig. 4 A' and B') unveil a much weaker H_2 oxidation functionality of the M5C1 catalyst, substantiating a close relationship between catalyst reducibility and oxidation activity. In particular, conversion values slightly increasing at lower reagents concentrations indicate an overall kinetic order lower than one (Fig. 4 A'), being also in this case consistent with fractional kinetic orders with respect to both reagents according to the influence of the H_2/O_2 ratio on

H_2 conversion (Fig. 4 B'). In fact, the kinetic analysis of rate data ($X < 15\%$) indicate reaction orders of 0.60 and 0.40 with respect to CO and O_2 , and of 0.76 and 0.1 with respect to H_2 and O_2 (Fig. S12 of SI), as shown by the empiric rate equations:

$$\text{rate}_{\text{CO}} = k_{\text{CO}} \cdot p_{\text{CO}}^{0.60} \cdot p_{\text{O}_2}^{0.40} \quad (4)$$

$$\text{rate}_{\text{H}_2} = k_{\text{H}_2} \cdot p_{\text{H}_2}^{0.76} \cdot p_{\text{O}_2}^{0.10} \quad (5)$$

According to DFT analysis, similar fractional kinetic orders mirror a comparable strength of CO and O_2 adsorption and a direct involvement of O_2 in the reaction cycle [29,31,33,34,50,51]. Instead, a reaction order closer to one mirrors the poor interaction of H_2 with the active Mn(IV) sites and, coupled to a kinetic order on O_2 close to zero, it reveals a Mark-van Krevelen (MvK) type mechanism characterised by much higher oxidation rate of active sites and negligible contribution of O_2 in the reaction path [29,50,51]. The different mechanistic clues of CO and H_2 oxidation are further confirmed by activation energy barriers of 41 ± 2 and $70 \pm 6 \text{ kJ} \cdot \text{mol}^{-1}$ (Fig. S12 of SI), satisfactorily mirroring the energy gap predicted by the SCM analysis ($\sim 35 \text{ kJ} \cdot \text{mol}^{-1}$). Indeed, both the matching of such values with the energy barriers of catalyst reduction (Fig. S12 of SI) and the coincidence of the onset reaction with catalyst reduction temperatures confirm that the catalyst-oxygen abstraction is a decisive step (r.d.s.) of both reaction pathways, as predicted by DFT calculations.

3.4. Activity-selectivity pattern under co-feeding conditions and reaction mechanisms

To rule out potential interferences of reaction cycles under co-feeding conditions, catalytic tests both in presence of CO and H_2 have been carried out. For the sake of comparison, these were run at the same conditions of CO and H_2 oxidation (GHSV, $180,000 \text{ h}^{-1}$), keeping constant the CO/ O_2 ratio (1.0) and varying the H_2/CO one between 10 and 60.

Fig. 5 A shows CO conversion data in the range of 293–433 K matching those in absence of H_2 , regardless of the H_2/CO ratio (Fig. 4A),

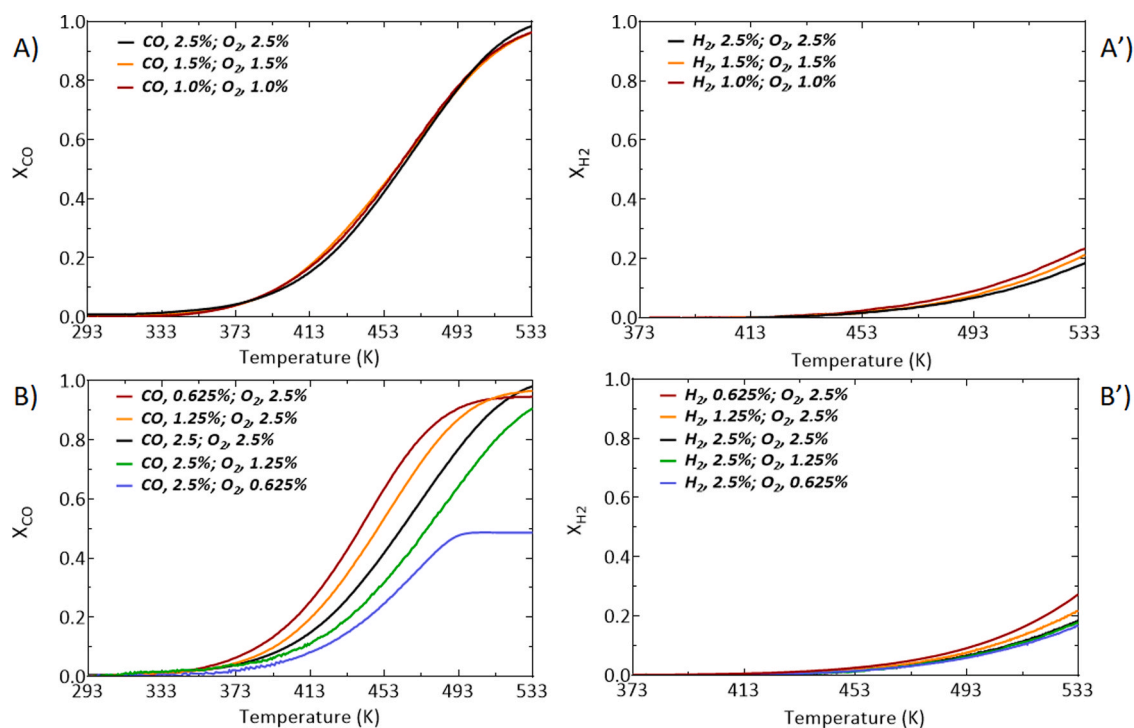


Fig. 4. CO (A, B) and H_2 (A', B') conversion data in the range of 293–533 K (P , 100 kPa) at different reagents concentration (CO/ O_2 and H_2/O_2 , 1) (A, A') and substrate/ O_2 ratio (B, B').

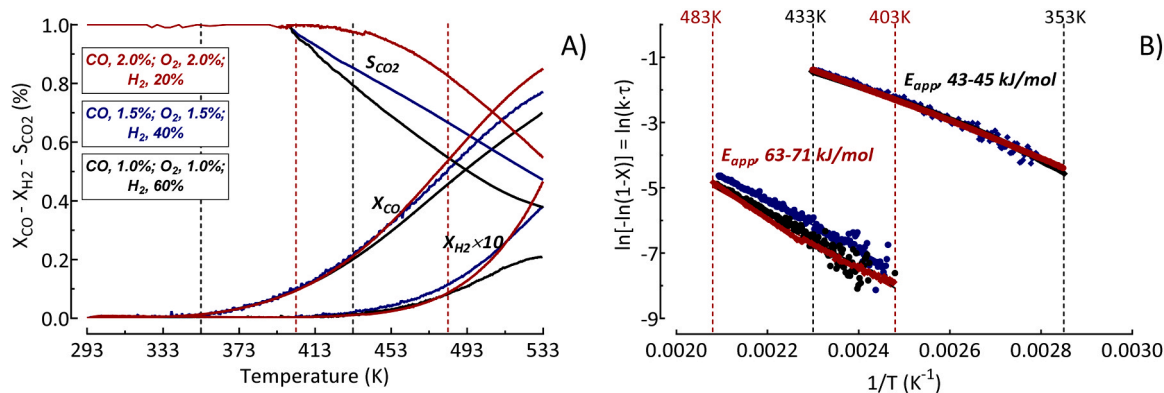


Fig. 5. (A) Activity-selectivity pattern of the M5C1 catalyst (P, 100 kPa) under CO and H₂ co-feeding conditions (the various colours refer to data at different conditions); (B) Arrhenius plots of the 1st-order kinetic constants of CO and H₂ oxidation.

while an incipient H₂ oxidation is noticed only at $T > 393$ K, similarly to that occurring in absence of CO (Fig. 4A').

This implies a full CO₂ selectivity in the range of 293–393 K, while at higher temperature the increasing H₂ oxidation rate causes a drop in the O₂ levels hindering both CO conversion and CO₂ selectivity consistently with the H₂/CO ratio (Fig. 5 A). Since the surface hydration is not relevant for the PROX behavior of the M5C1 catalyst because of very low H₂ oxidation rate at $T < 393$ K, the apparent activation energies match the values previously recorded for CO and H₂ oxidation alone (Fig. 5 B), ruling out any mutual effect under co-feeding conditions.

Thus, theoretical and experimental evidences lead to sketch the following reaction mechanisms.

CO oxidation: in agreement with the essential clues of DFT analysis (Fig. 1), the CO oxidation cycle can be described by five essential reaction steps (Sch. 1) [29,31–34]. These include CO adsorption on the Mn(IV) site (a) prompting the formation of a “bridged” carbonate intermediate evolving into the 1st CO₂ molecule by the abstraction of O-atoms (b); the oxygen-vacancy triggers the co-adsorption of O₂ (c) and CO (d), forming a “bidentate” carbonate intermediate that gives the 2nd CO₂ molecule and the replenishment of the Mn(IV) site (e) [31–34]. Thus, while the decisive role of catalyst oxygen (r.d.s.) could infer a classical MvK mechanism involving lattice oxygen atoms, the inhibiting kinetic effect of CO₂ and the involvement of adsorbed oxygen species are rather compatible with a L-H type path, prompted by the reactivity of the Mn(IV)-O bonds towards CO [29–34,51,52]. In fact, previous CO “pulse-reaction” tests and “steady-state O₂-chemisorption” measurements documented a negligible reactivity of lattice oxygen species and a fully oxidized status of the catalyst at steady-state reaction conditions (T , 393 K) [31], supporting the evidence that the reduction of active Mn(IV) sites determines the CO oxidation kinetics [27,29,31–34]. In fact, the classical MvK path is predominant at $T > 523$ K, when the lattice oxygen mobility of MnO_x catalysts is fast enough to sustain the oxidation of adsorbed CO [52].

H₂ oxidation: a reaction order slightly lower than one (Eq. (5)) confirms that some weak surface interaction sparks the H₂ oxidation on the M5C1 catalyst. According to DFT data (Fig. 2), this interaction should encompass diatomic oxygen species on “over-oxidized” Mn sites, mimicking the O₂-Mn₄O₇ intermediate (*v. supra*). Under co-feeding conditions these are generated by the CO oxidation cycle, but a considerably higher energy barrier (ΔE , 30–35 kJ·mol⁻¹) determines H₂ oxidation probabilities lower by orders of magnitude in the investigated range of temperature. However, unchanging activation energies reveal that the H₂ oxidation proceeds via the same mechanism irrespective of CO and O₂ (H₂-TPR), pointing to the occurrence of oxygen spillover processes triggering the genesis of O₂-M₄O₇ sites under anaerobic conditions. This implies that the surface oxygen mobility controls the H₂ oxidation activity of the *real* catalyst. Although the dismutation of Mn(IV) atoms belonging to different clusters was not inspected by DFT

analysis, it must be noticed that this property is crucial for the reactivity of bare and promoted MnO₂ catalysts, together with the availability and local environment of Mn(IV) sites [46–49,53–55].

Depending on active phase structure and dispersion, the TPD analysis of the M5C1 catalyst displays a peculiar O₂ desorption profile in the range of 293–1073 K, accounting for an overall release of $\sim 3 \cdot 10^{-3}$ mol_{O₂}·g⁻¹ that is diagnostic of the MnO₂→MnO_{1.33} phase transition (Fig. 6). In particular, the flex at 763 K and the maximum at 862 K are due to the breakage of unsaturated Mn–O bonds from surface Mn(IV) atoms, while the sharp maximum at 921 K monitors the lattice oxygen release accounting for the Mn₂O₃→Mn₃O₄ transition [31,33,53–55]. Moreover, a small peak (<1%) in the range of 293–473 K monitors the release of oxygen species weakly adsorbed onto surface defects and oxygen-vacancies, which are generally associated with lower oxidation states of Mn and/or Ce atoms [46,47,53–55]. Although these could adsorb O₂ enhancing the oxidation functionality of Mn(IV) sites [30],

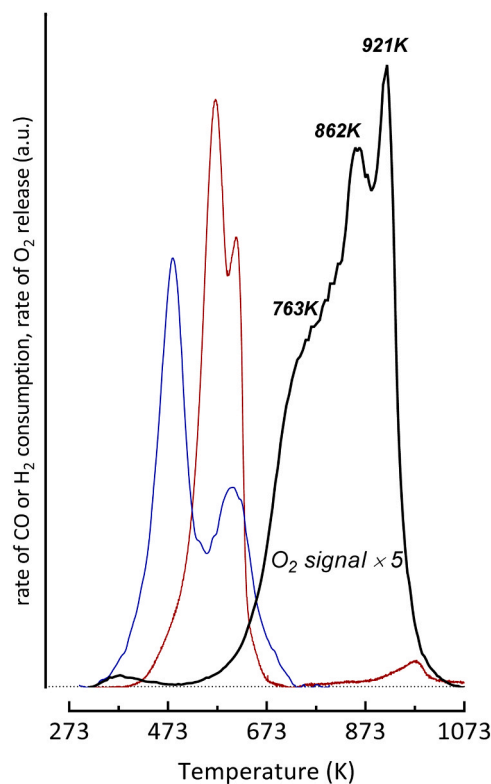


Fig. 6. Comparison of the O₂-TPD profile (black line) with the CO-TPR (blue line) and H₂-TPR (red line) patterns of the M5C1 catalyst.

the H₂-TPR analysis shows negligible changes in the reduction pattern of the M5C1 catalyst after an in situ treatment at 673 K and subsequent cooling in O₂ flow (Fig. S11 of SI), unveiling a negligible influence of such sites on the O₂ adsorption properties of the M5C1 catalyst. At variance, the oxygen mobility probed by TPD analysis suggests that such sites could favour the spillover of O-atoms, prompting the formation of O-vacancies and diatomic oxygen species also at low temperature. According to DFT data, the latter would spark the H₂ oxidation (Fig. 2) although high energy barriers shift the formation of water due to reduction of Mn(IV) sites at $T \geq 373$ K (Fig. 6) [46,47,49,52–55]. Notably, these clues match literature findings documenting direct relationships between the energy of O-vacancy formation and the H₂ surface reduction rate of various MnO₂ polymorphs [49] and α -MnO₂ samples exposing different crystal facets [53], suggesting a mechanism of four reaction steps for H₂ oxidation (Sch. 2): (a') the preliminary formation of adsorbed O₂ species (i.e., O₂-Mn₄O₇) and the consequent H₂ adsorption (b'), followed by the formation of water and replenishment of Mn(IV) site (c'). These three steps produce an O-vacancy accounting for the reduction of surface Mn(IV) atoms in absence of oxygen (i.e., H₂-TPR), while the regeneration of O₂-Mn₄O₇ sites (d') would explain the small kinetic effect of O₂ under reaction conditions (Fig. S12B' of SI). Scheme 1 and 2.

3.5. Preferential CO oxidation (PROX) pattern

The typical PROX behavior pattern recorded under kinetic regime prompted us to inspect the performance of the M5C1 catalyst under integral conversion conditions for practical purposes. In particular, at a GHSV of 3600 h⁻¹ (1 g_{cat}) it ensures CO conversion values of 35% and 60% at 353 and 373 K respectively, and CO₂ selectivity levels of 100% (Fig. 7 A). At $T > 393$ K the rising H₂ conversion causes a progressive decrease of the CO₂ selectivity and a drop of O₂ concentration hindering the complete CO conversion. Even if these data signal the incipient occurrence of mass-transfer constraints [26,31,33], lowering further the GHSV (720 h⁻¹) the CO conversion increases to 94% and 99% at 353 and 373 K respectively, while selectivity values of 100% and 95% are still recorded (Fig. 7 A). Therefore, at 373 K the M5C1 catalyst almost fulfills the targets of the PROX process for PEMFC devices, owing to a residual CO concentration lower than 100 ppm and H₂ loss lower than 0.2%, corresponding to a three orders of magnitude different oxygen-utilization factor (i.e., $k_{CO}/k_{H_2} \sim 10^3$), considering a H₂/CO ratio of 85. Furthermore, despite the increasing H₂ conversion in the range of 393–423 K causes a progressive decay of the CO₂ selectivity from 71% to a minimum value of 50%, the PROX behavior of the M5C1 catalyst is also better at $T > 373$ K since a full CO conversion is accompanied by H₂ loss lower than 1% due to the excess of O₂ (0.5%). Under such conditions the M5C1 catalyst is also stable (Fig. 7B), keeping at 363 K constant conversion (93–97%) and selectivity (95–97%) levels in 72 h of reaction time.

Finally, we probed the performance of the M5C1 catalyst under realistic process conditions, mimicking a WGS feedstock by adding H₂O (4%) and CO₂ (10%) in the reaction stream. Fig. 7 C shows significant negative effects of H₂O and CO₂ feeding on CO conversion [33,52], although selectivity values of 100% are still observed at $T \leq 373$ K. In particular, at 353 and 373 K water causes a drop in activity probed by CO conversion values of 20% and 60%, respectively. Considering the

constant CO conversion (94–100%) at such temperatures in absence of water (Fig. 7 A), these data would signal a growth of the energy barrier by 70 kJ·mol⁻¹ that well compares with the desorption energy (~ 72 kJ·mol⁻¹) of water from the Mn₄O₈ cluster. At 393 K conversion and selectivity values are equal to 96% and 95% respectively, while at higher temperatures a full CO conversion is accompanied by selectivity values of 55%.

Adding both water and CO₂ in the reaction stream, CO conversion at 353 and 373 K lowers to 10% and 40%, indicating a further growth of the apparent activation barrier by ca. 10 kJ·mol⁻¹ [33]. At 393 K the CO conversion attains a level of 82% with a CO₂ selectivity of 92%, while at $T \geq 413$ K a complete CO conversion and CO₂ selectivity values of 50% substantiate the PROX behavior of the M5C1 catalyst under realistic process conditions. This is corroborated by fairly reproducible conversion-selectivity data throughout three reaction cycles in the range of 393–423 K, which is preliminarily diagnostic also of a substantial catalyst stability.

4. Conclusions

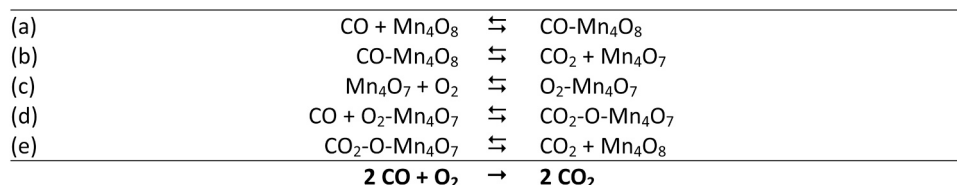
The CO and H₂ oxidation functionality of Mn(IV) sites has been assessed by DFT analysis of adsorption and activation energies on a model Mn₄O₈ cluster in presence and absence of O₂. A MnCeO_x catalyst (M5C1) with large availability of Mn(IV) sites has been investigated as experimental counterpart of the model Mn₄O₈ cluster. According to DFT predictions, the M5C1 catalyst shows a remarkable CO oxidation performance at $T \geq 293$ K and no H₂ oxidation activity at $T < 373$ K. The reducibility of Mn(IV) sites controls both the CO and H₂ oxidation activity of the M5C1 catalyst. CO oxidation occurs via a stepwise path involving both catalyst and gas phase oxygen, while the H₂ oxidation requires the interaction with diatomic oxygen species. High activation energy barriers hinder H₂ oxidation favoring the PROX performance of the M5C1 catalyst. The M5C1 catalyst ensures a complete CO removal with H₂ loss lower than 1% in the range of 353–423 K. Despite moderate inhibiting effects of water and CO₂ co-feeding, MnO₂ materials can be considered as effective, low cost and robust PROX catalysts. Further theoretical and experimental studies for the optimization of the PROX performance of MnO_x-based catalysts are currently in progress.

CRedit authorship contribution statement

Francesco Arena: Conceptualization, Methodology, Writing, Supervision. **Francesco Ferrante:** Methodology, Experimental investigation and data curation, Writing. **Roberto Di Chio:** Experimental investigation and data curation, Writing – original draft. **Giuseppe Bonura:** Experimental investigation, Data curation; **Francesco Frusteri:** Data elaboration, Supervision; **Leone Frusteri:** Experimental investigation, Data curation; **Antonio Prestianni:** Experimental investigation, Data curation. **Sara Morandi:** Experimental investigation, Data curation. **Gianmario Martra:** Methodology, Conceptualization. **Dario Duca:** Conceptualization, Writing, Supervision.

Declaration of Competing Interest

The authors declare that they have no known competing financial interests or personal relationships that could have appeared to influence



Scheme 1. Catalytic cycle of the CO oxidation.

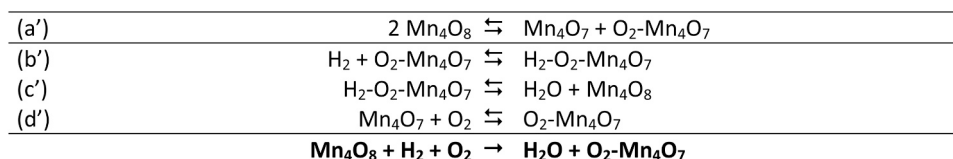
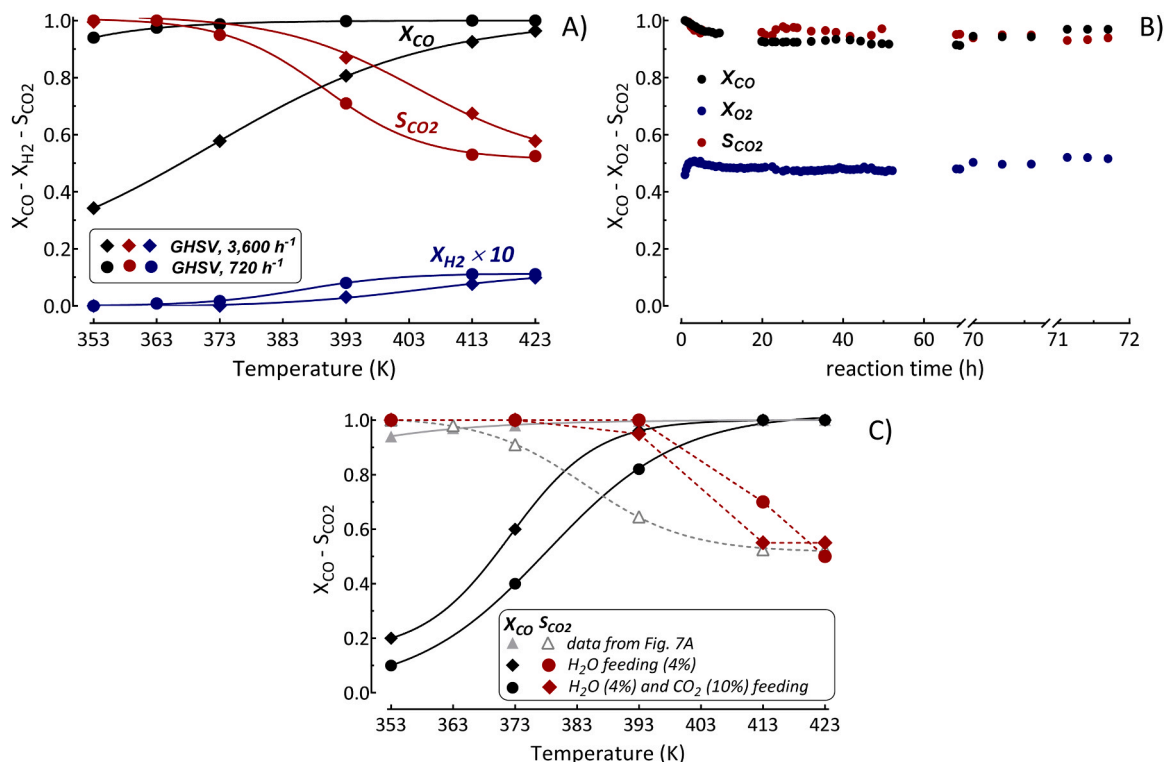
Scheme 2. Catalytic cycle of the H_2 oxidation.

Fig. 7. (A) PROX pattern of the M5C1 catalyst at different GHSV (P, 100 kPa; CO , 1%; O_2 , 1%; H_2 , 85%; N_2 , 13%); (B) stability test at 363 K (GHSV of 720 h⁻¹); (C) Effect of H_2O (4%) and CO_2 (10%) in the feed on the PROX performance (GHSV, 720 h⁻¹; P, 100 kPa; CO , 1%; O_2 , 1%; H_2 , 70%; N_2 , 14%).

the work reported in this paper.

Appendix A. Supporting information

Supplementary data associated with this article can be found in the online version at [doi:10.1016/j.apcatb.2021.120715](https://doi.org/10.1016/j.apcatb.2021.120715).

References

- [1] A.F. Ghenciu, Review of fuel processing catalysts for hydrogen production in PEM fuel cell systems, *Curr. Opin. Solid State Mater. Sci.* 6 (2002) 389–399.
- [2] K. Liu, A. Wang, T. Zhang, Recent advances in preferential oxidation of CO reaction over platinum group metal catalysts, *ACS Catal.* 2 (2012) 1165–1178.
- [3] P. Jing, X. Gong, B. Liu, J. Zhang, Versatile nanoplatforms with enhanced photodynamic therapy: designs and applications, *Theranostics* 10 (2020) 7287–7318.
- [4] D. Li, Y. Zhu, H. Wang, Y. Ding, Nanoporous gold as an active low temperature catalyst toward CO oxidation in hydrogen-rich stream, *Sci. Rep.* 3 (2013) 3015.
- [5] G.P. Sousa, C.S. de Oliveira, E.T. Neto, F.A. Sigoli, I.O. Mazali, Au–CeO₂-based nanocatalysts supported on SBA-15 for preferential oxidation of carbon monoxide (PrOx-CO), *N. J. Chem.* 44 (2020) 19028–19036.
- [6] D. Widmann, R.J. Behm, Activation of molecular oxygen and the nature of the active oxygen species for CO oxidation on oxide supported Au catalysts, *Acc. Chem. Res.* 47 (2014) 740–749.
- [7] A.U. Nilekar, S. Alayoglu, B. Eichhorn, M. Mavrikakis, Preferential CO oxidation in hydrogen: reactivity of core-shell nanoparticles, *J. Am. Chem. Soc.* 132 (2010) 7418–7428.
- [8] L. Cao, W. Liu, Q. Luo, R. Yin, B. Wang, J. Weissenrieder, M. Soldemo, H. Yan, Y. Lin, Z. Sun, C. Ma, W. Zhang, S. Chen, H. Wang, Q. Guan, T. Yao, S. Wei, J. Yang, J. Lu, Atomically dispersed iron hydroxide anchored on Pt for preferential oxidation of CO in H_2 , *Nature* 565 (2019) 631–635.
- [9] H. Guan, J. Lin, L. Li, X. Wang, T. Zhang, Highly active subnano Rh/Fe(OH)_x catalyst for preferential oxidation of CO in H_2 -rich stream, *Appl. Catal. B: Environ.* 184 (2016) 299–308.
- [10] H. Zhang, X. Liu, N. Zhang, J. Zheng, Y. Zheng, Y. Li, C.-J. Zhong, B.H. Chen, Construction of ultrafine and stable PtFe nano-alloy with ultra-low Pt loading for complete removal of CO in PROX at room temperature, *Appl. Catal. B: Environ.* 180 (2016) 237–245.
- [11] H. Xu, Q. Fu, Y. Yao, X. Bao, Highly active Pt-Fe bicomponent catalysts for CO oxidation in the presence and absence of H_2 , *Energy Environ. Sci.* 5 (2012) 6313–6320.
- [12] G. Chen, Y. Zhao, G. Fu, P.N. Duchesne, L. Gu, Y. Zheng, X. Weng, M. Chen, P. Zhang, C.W. Pao, J.F. Lee, N. Zheng, Interfacial effects in iron-nickel hydroxide-platinum nanoparticles enhance catalytic oxidation, *Science* 344 (2014) 495–499.
- [13] Y. Pan, S.Y. Hwang, X. Shen, J. Yang, J. Zeng, M. Wu, Z. Peng, Computational-guided development of platinum alloy catalyst for carbon monoxide preferential oxidation, *ACS Catal.* 8 (2018) 5777–5786.
- [14] X. Liao, Y. Liu, W. Chu, S. Sall, C. Petit, V. Pitchon, V. Caps, Promoting effect of AuCu alloying on Au-Cu/CeO₂-catalyzed CO oxidation: a combined kinetic and in situ DRIFTS study, *J. Catal.* 382 (2020) 329–338.
- [15] S. Cao, Y. Zhao, S. Lee, S. Yang, J. Liu, G. Giannakakis, M. Li, M. Ouyang, D. Wang, E.C.H. Sykes, M. Flytzani-Stephanopoulos, High-loading single Pt atom sites [Pt-O(OH)₂] catalyze the CO PROX reaction with high activity and selectivity at mild conditions, *Sci. Adv.* 6 (2020) 3809.
- [16] Y. Chen, J. Lin, L. Li, X. Pan, X. Wang, T. Zhang, Effects of land use and land cover on soil erosion control in southern China: implications from a systematic quantitative review, *J. Environ. Manag.* 282 (2021), 111924.
- [17] J. Cai, Z. Liu, K. Cao, Y. Lang, S. Chu, B. Shan, R. Chen, Highly dispersed Pt studded on CoO_x nanoclusters for CO preferential oxidation in H_2 , *J. Mater. Chem. A* 8 (2020) 329–338.
- [18] S. Huang, K. Hara, A. Fukuoka, Green catalysis for selective CO oxidation in hydrogen for fuel cell, *Energy Environ. Sci.* 2 (2009) 1060–1068.
- [19] J. Lu, J. Wang, Q. Zou, D. He, L. Zhang, Z. Xu, S. He, Y. Luo, Unravelling the nature of the active species as well the doping effect over Cu/Ce-based catalyst for carbon monoxide preferential oxidation, *ACS Catal.* 9 (2019) 2177–2185.

- [20] Y.-I. Hasegawa, R.-U. Maki, M. Sano, T. Miyake, Preferential oxidation of CO on copper-containing manganese oxides, *Appl. Catal. A Gen.* 371 (2009) 67–72.
- [21] V.D.B.C. Dasireddy, B. Likozar, J. Valand, Preferential oxidation of CO in $H_2/H_2O/CO_2$ water–gas shift feedstocks over Cu-based carbon nanotubes-supported heterogeneous catalysts, *Appl. Catal. B Environ.* 237 (2018) 687–697.
- [22] V.D.B. Dasireddy, J. Valand, B. Likozar, PROX reaction of CO in $H_2/H_2O/CO_2$ Water-Gas Shift (WGS) feedstocks over Cu-Mn/ Al_2O_3 and Cu-Ni/ Al_2O_3 catalysts for fuel cell applications, *Renew. Energy* 116 (2018) 75–87.
- [23] L. Zhong, T. Kropp, W. Baaziz, O. Ersen, D. Teschner, R. Schlögl, M. Mavrikakis, S. Zafeiratos, Correlation between reactivity and oxidation state of cobalt oxide catalysts for CO preferential oxidation, *ACS Catal.* 9 (2019) 8325–8334.
- [24] L. Zhong, M. Barreau, D. Chen, V. Caps, M. Haevecker, D. Teschner, D.H. Simonne, E. Borfecchia, W. Baaziz, B. Smid, S. Zafeiratos, Effect of manganese promotion on the activity and selectivity of cobalt catalysts for CO preferential oxidation, *Appl. Catal. B Environ.* 297 (2021), 120397.
- [25] Y. Bu, S. Er, J.W. Niemantsverdriet, H.O.A. Fredriksson, Preferential oxidation of CO in H_2 on Cu and Cu/CeO₂ catalysts studied by in situ UV-Vis and mass spectrometry and DFT, *J. Catal.* 357 (2018) 176–187.
- [26] F. Arena, R. Di Chio, B. Fazio, C. Espro, L. Spiccia, A. Palella, L. Spadaro, Probing the functionality of nanostructured MnCeO_x catalysts in the carbon monoxide oxidation. Part I. Influence of cerium addition on structure and CO oxidation activity, *Appl. Catal. B Environ.* 210 (2017) 14–22.
- [27] S. Liang, F. Teng, G. Bulgan, R. Zong, Y. Zhu, Effect of phase structure of MnO₂ nanorod catalyst on the activity for CO oxidation, *J. Phys. Chem. C* 112 (2008) 5307–5315.
- [28] K. Li, J. Chen, Y. Peng, W. Lin, T. Yan, J. Li, The relationship between surface open cells of α -MnO₂ and CO oxidation ability from a surface point of view, *J. Mater. Chem. A* 5 (2017) 20911–20921.
- [29] J. Gao, C. Jia, L. Zhang, H. Wang, Y. Yang, S.-F. Hung, Y.-Y. Hsu, B. Liu, Tuning chemical bonding of MnO₂ through transition-metal doping for enhanced CO oxidation, *J. Catal.* 341 (2016) 82–90.
- [30] F. Arena, R. Di Chio, A. Palella, L. Spadaro, L. Frusteri, B. Fazio, S. Morandi, G. Martra, Tailoring manganese oxide catalysts for the total oxidation of pollutants in gas and liquid phase, *Appl. Catal. A Gen.* 610 (2021), 117917.
- [31] F. Arena, R. Di Chio, L. Filicetto, G. Trunfio, C. Espro, A. Palella, A. Patti, L. Spadaro, Probing the functionality of nanostructured MnCeO_x catalysts in the carbon monoxide oxidation. Part II. Reaction mechanism and kinetic modelling, *Appl. Catal. B Environ.* 218 (2017) 803–809.
- [32] L.C. Hsu, M.-K. Tsai, Y.-H. Lu, H.-T. Chen, Computational investigation of CO adsorption and oxidation on Mn/CeO₂(111) Surface, *J. Phys. Chem. C* 117 (2013) 433–441.
- [33] F. Arena, R. Di Chio, C. Espro, A. Palella, L. Spadaro, A definitive assessment of the CO oxidation pattern of a nanocomposite MnCeO_x catalyst, *React. Chem. Eng.* 3 (2018) 293–300.
- [34] F. Arena, R. Di Chio, C. Espro, B. Fazio, A. Palella, L. Spadaro, A new class of MnCeO_x materials for the catalytic gas exhausts emission control: a study of the CO model compound oxidation, *Top. Catal.* 62 (2019) 259–265.
- [35] F. Arena, B. Gumina, A.F. Lombardo, C. Espro, A. Patti, L. Spadaro, L. Spiccia, Nanostructured MnO_x catalysts in the liquid phase selective oxidation of benzyl alcohol with oxygen: Part I. Effects of Ce and Fe addition on structure and reactivity, *Appl. Catal. B Environ.* 162 (2015) 260–267.
- [36] L. Gueci, F. Ferrante, A. Prestianni, R. Di Chio, A.F. Patti, D. Duca, F. Arena, DFT insights into the oxygen-assisted selective oxidation of benzyl alcohol on manganese dioxide catalysts, *Inorg. Chim. Acta* 511 (2020), 119812.
- [37] M.J. Frisch, G.W. Trucks, H.B. Schlegel, G.E. Scuseria, M.A. Robb, J.R. Cheeseman, G. Scalmani, V. Barone, B. Mennucci, G.A. Petersson, H. Nakatsuji, M. Caricato, X. Li, H.P. Hratchian, A.F. Izmaylov, J. Bloino, G. Zheng, J.L. Sonnenberg, M. Hada, M. Ehara, K. Toyota, R. Fukuda, J. Hasegawa, M. Ishida, T. Nakajima, Y. Honda, O. Kitao, H. Nakai, T. Vreven, J.J. A. Montgomery, J.E. Peralta, F. Ogliaro, M. Bearpark, J.J. Heyd, E. Brothers, K.N. Kudin, V.N. Staroverov, R. Kobayashi, J. Normand, K. Raghavachari, A. Rendell, J.C. Burant, S.S. Iyengar, J. Tomasi, M. Cossi, N. Rega, J.M. Millam, M. Klene, J.E. Knox, J. B. Cross, V. Bakken, C. Adamo, J. Jaramillo, R. Gomperts, R.E. Stratmann, O. Yazyev, A.J. Austin, R. Cammi, C. Pomelli, J.W. Ochterski, R.L. Martin, K. Morokuma, V.G. Zakrzewski, G.A. Voth, P. Salvador, J.J. Dannenberg, S. Dapprich, A.D. Daniels, Ö. Farkas, J.B. Foresman, J.V. Ortiz, J. Cioslowski, D.J. Fox, Gaussian 09 Revision D.01", gaussian Inc. Wallingford CT 2009.
- [38] Y. Zhao, D.G. Truhlar, A new local density functional for main-group thermochemistry, transition metal bonding, thermochemical kinetics, and noncovalent interactions, *J. Chem. Phys.* 125 (2006), 194101.
- [39] M. Dolg, U. Wedig, H. Stoll, H. Preuss, Energy-adjusted ab initio pseudopotentials for the first row transition elements, *J. Chem. Phys.* 86 (1987) 866–872.
- [40] Y. Zhao, D.G. Truhlar, The M06 suite of density functionals for main group thermochemistry, thermochemical kinetics, noncovalent interactions, excited states, and transition elements: two new functionals and systematic testing of four M06-class functionals and 12 other functionals, *Theor. Chem. Acc.* 120 (2008) 215–241.
- [41] Y. Sun, H. Chen, Performance of density functionals for activation energies of Zr-mediated reactions, *J. Chem. Theory Comp.* 9 (2013) 4735–4743.
- [42] Y. Sun, H. Chen, Performance of density functionals for activation energies of Re-catalyzed organic reactions, *J. Chem. Theory Comp.* 10 (2014) 579–588.
- [43] L. Hu, H. Chen, Assessment of DFT methods for computing activation energies of Mo/W-mediated reactions, *J. Chem. Theory Comp.* 11 (2015) 4601–4614.
- [44] J.A. Christiansen, The elucidation of reaction mechanisms by the method of intermediates in quasi-stationary concentrations, *Adv. Cat.* 5 (1953) 311–353.
- [45] S. Kozuch, S. Shaik, A combined kinetic-quantum mechanical model for assessment of catalytic cycles: application to cross-coupling and heck reactions, *J. Am. Chem. Soc.* 128 (2005) 3355–3365.
- [46] L. Zhu, J. Wang, S. Rong, H. Wang, P. Zhang, Cerium modified birnessite-type MnO₂ for gaseous formaldehyde oxidation at low temperature, *Appl. Catal. B Environ.* 211 (2017) 212–221.
- [47] W. Yang, Y. Zhu, F. You, L. Yan, Y. Ma, C. Lu, P. Gao, Q. Hao, W. Li, Insights into the surface-defect dependence of molecular oxygen activation over birnessite-type MnO₂, *Appl. Catal. B Environ.* 233 (2018) 184–193.
- [48] X. Wang, Y. Li, Synthesis and formation mechanism of manganese dioxide nanowires/nanorods, *Chem. Eur. J.* 9 (2003) 300–306.
- [49] E. Hayashi, Y. Yamaguchi, K. Kamata, N. Tsunoda, Y. Kumagai, F. Oba, M. Hara, Effect of MnO₂ crystal structure on aerobic oxidation of 5-hydroxymethylfurfural to 2,5-furan-dicarboxylic acid, *J. Am. Chem. Soc.* 141 (2019) 890–900.
- [50] M. Schaub, R. Merkle, J. Maier, Interdependence of point defects and reaction kinetics: CO and CH₄ oxidation on Ceria and Zirconia, *J. Phys. Chem. C* 124 (2020) 18544–18556.
- [51] M.A. Vannice, An analysis of the Mars–van Krevelen rate expression, *Catal. Today* 123 (2007) 18–22.
- [52] K. Ramesh, L. Chen, F. Chen, Y. Liu, Z. Whang, Y.-F. Han, Re-investigating the CO oxidation mechanism over unsupported MnO, Mn₂O₃ and MnO₂ catalysts, *Catal. Today* 131 (2008) 477–482.
- [53] S. Rong, P. Zhang, F. Liu, Y. Yang, Engineering crystal facet of α -MnO₂ nanowire for highly efficient catalytic oxidation of carcinogenic airborne formaldehyde, *ACS Catal.* 8 (2018) 3435–3446.
- [54] L. Xueting, L. Shujun, H. Hui, W. Junliang, C. Limin, Y. Daiqi, F. Mingli, Evolution of oxygen vacancies in MnO_x-CeO₂ mixed oxides for soot oxidation, *Appl. Catal. B Environ.* 223 (2018) 91–102.
- [55] S. Mo, Q. Zhang, J. Li, Y. Sun, Q. Ren, S. Zou, Q. Zhang, J. Lu, M. Fu, D. Mo, J. Wu, H. Huang, D. Ye, Highly efficient mesoporous MnO₂ catalysts for the total toluene oxidation: oxygen-vacancy defect engineering and involved intermediates using in situ DRIFTS, *Appl. Catal. B Environ.* 264 (2020), 118464.